3D prostate elastography: algorithm, simulations and experiments

3D prostate elastography: algorithm, simulations and experiments

A V Patil, C D Garson and J A Hossack

Biomedical Engineering, University of Virginia, Charlottesville, VA 22903, USA

E-mail: avp2b@virginia.edu

Abstract
A multi-resolution hybrid strain estimator is presented. The estimator is locally
initialized by the B-mode tracking stage. Nonlinear and linear stretching
regimes are applied in successive RF tracking stages for refining the estimated
axial and lateral displacements. A staggering operator is used to derive the
strain images from the reconstructed axial displacements. Simulations and
experiments, conducted at a center frequency of 12 MHz, 40% fractional
bandwidth, on a 128 element transducer with 0.2 mm pitch, with elastographic
window length of 2 mm and overlap of 90%, demonstrate a 3–6 dB improvement
in the elastographic contrast-to-noise ratio over the results obtained using
conventional multi-stage stretching based strain estimators. The average
image cross-correlation coefficient obtained using the proposed algorithm was
improved by 6–8%. 3D elastographic simulations conducted to study the
performance of a 3D elastographic imaging framework predict achievable axial
and lateral resolutions of approximately five and ten wavelengths, respectively.
A close correspondence between inclusions reconstructed from experimental
elastograms and the known physical shape of actual 3D inclusions demonstrates
the potential application of 3D elastography for identifying and classifying the
detected lesions (invisible in sonograms) on the basis of their shape.

(Some figures in this article are in colour only in the electronic version)

1. Introduction

Adenocarcinoma of the prostate is the second most common cause of cancer specific deaths
in North American men. Each year, there are 220 000 new cases of prostate cancer and 50 121
prostate cancer related deaths (American Cancer Society 2006). A variety of approaches are
used for detecting prostate cancer. These approaches include: digital rectal examination, the
use of serum prostate specific antigen (PSA) and trans-rectal ultrasound. PSA indicates the
presence or absence of prostate cancer but provides very limited information on the location,

size and type of the tumor. PSA (using a cutoff of approximately 4–10 ng ml^{-1}) has sensitivity and specificity of approximately 63–83% (Souchon *et al* 2005). Digital rectal examination is a subjective approach and fails to detect smaller lesions deep in the prostate tissue. Potdevin *et al* (2000) used quantitative measurements from Doppler flow ultrasound to discriminate cancers from normal prostate tissue. Trans-rectal ultrasound in the form of texture analysis of B-mode images (Sheppard and Shih 2005) and neural network based multivariate analysis of backscattered ultrasound data (Fellepa *et al* 2001) have been explored as means to detect and classify prostate cancers. However, clinical studies by Elkis and Brawer (1994) demonstrated significant occurrences of cancerous prostate tissue as iso-echoic regions in B-mode images, which cast doubts on the efficacy of texture analysis of B-mode data for prostate cancer detection and classification. The sensitivity of trans-rectal ultrasound, in general, ranges from 71 to 92% for cancers and 60 to 85% for sub-clinical diseases. The specificity ranges from 49 to 79% with positive predicted values (ppv) of approximately 30% (Waterhouse and Resnick 1989). Contrast enhanced ultrasound has been successfully used to improve the sensitivity of cancer detection of the prostate (26% baseline improved to 42% using contrast enhancement (Halpern *et al* 2002)). Contrast agents, however, are not used widely in the clinical environment due to their cost and lack of regulatory approval/reimbursement.

An alternate approach to the detection of cancers in tissue is by imaging the mechanical properties of the tissue. It is well known that pathological changes in the tissue are correlated with changes in the tissue mechanical properties (Krouskop *et al* 1998). Elastography (Ophir *et al* 1991, O'Donnell *et al* 1994) is an ultrasound based imaging technique, which uses remote palpation or quasi-static compression for imaging the tissue elasticity. In elastography, the pre- and post-compression echo radio frequency (RF) data are tracked to produce an internal tissue displacement image, the gradient of which produces a strain image. Previous work on prostate elastography has reported sensitivity of 76% and specificity of 84% with positive predicted values in the range of approximately 50% (Pesavento and Lorenz 2001). Other researchers have reported the use of elastography for monitoring thermal (prostate) lesions during high intensity focused ultrasound (HIFU) therapy (Souchon *et al* 2005). Primarily, elastography has been established as a technique which can effectively detect hard lesions in relatively soft backgrounds with spatial resolution as fine as a few wavelengths of the insonation pulse used for imaging the tissue (Righetti *et al* 2002). However, the secondary objective of elastography is to classify detected lesions as malignant or benign, which can potentially prevent unnecessary biopsies. It is well known that malignant lesions exhibit irregular shapes that are strikingly different from those of benign lesions, which are relatively smooth and approximately spherical (Ueno 1986). As a result, malignant lesions are more thoroughly integrated with the host tissue than the benign lesions. Thus, malignant lesions, in response to external displacement, undergo less shear motion than benign lesions. Investigators are working on using this principle for discriminating malignant from benign lesions by imaging the shear strain induced in the tissue in response to the external stimulus (Techavipoo *et al* 2004). However, simulations and experiments conducted by Thitaikumar *et al* (2005) suggest that the upper bound on the signal-to-noise ratio (SNR) of the shear strain elastograms is approximately an order of magnitude lower than that of the axial strain elastograms, limiting the efficacy of such a technique *in vivo* where patient motion may be substantial enough to degrade the contrast-to-noise ratio of the acquired shear strain image (Bilgen and Insana **?**). Additionally, when the modulus contrast between the lesions and the background is low (e.g. prostate cancer, for which the modulus ratio is $\leqslant 4$ (Krouskop *et al* 1998)) lesion mobility assessment using shear strain measurement is challenging. Clinical studies conducted by Garra *et al* (1997) have successfully demonstrated that the shape of malignant lesions (in elastograms) in breast tissue is different from that of benign lesions and may be used

as a distinctive feature for classification of lesions. One approach to maximize information obtained from the axial strain image is to generate volumetric axial strain elastograms using a two-dimensional transducer array or a modified one-dimensional 'I-Beam' (Hossack *et al* 2002) transducer array capable of estimating elevational motion.

In this paper, we present a hybrid strain estimation algorithm, which generates axial and lateral displacements (strain images) corrected for elevational motion, 3D elastographic simulations, and phantom experiments. We use the algorithm to demonstrate the ability of axial strain elastography to reconstruct different 3D shapes (Bilgen *et al* 2003).

2. Materials and methods

2.1. 3D Elastographic simulation framework

All simulations were conducted using a 3D elastographic simulation framework similar to that proposed by Nightingale *et al* (2000) and Patil *et al* (2007). Patil *et al* used a 3D shift-invariant convolution model for generating the pre- and post compression echo RF data. In this work, we have used a more realistic Field II simulation model (Jensen and Nikolov 2000) for echo RF data generation, as it takes into account the frequency-dependent attenuation, and simulates realistic diffraction patterns for a given array geometry. Most FEA simulations performed by Patil *et al* were restricted by the assumption of uniform boundary conditions, which is not strictly valid for trans-rectal prostate elastography. In this work, all FEA simulations were performed using non-uniform[1] boundary conditions. Figure 1 illustrates the flow chart of the simulation framework used in this work. As illustrated in the figure, the FEA model is used to generate displacement fields with desired boundary conditions. The displacement fields are used to calculate new scatterer positions due to applied compression. The 'calc_scat' function from FIELD II is used to generate the pre- and the post-compression RF data. This RF data can then be tracked to reconstruct the internal displacement field and the induced strain. Ideal strain images can be directly obtained from the FEA software, and are used to compare the quality of reconstructed elastograms.

ANSYS (Canonsburg, PA), a finite element analysis (FEA) simulation software package, was used in this work. Arbitrary regions of interest (ROI's) can be created within the FEA model by changing the local material properties (shear modulus, material density, etc). A fine FEA mesh (approximately 13 FEA nodes per resolution cell) results in accurate parameter estimation (3D internal displacement, in this case). Boundary conditions (applied displacement) can be applied to an object surface, an object element or a node of the object element (after meshing). The internal object deformation due to the applied displacement is then estimated by solving the associated partial differential equations numerically. In this work, a preconditioned conjugate gradient iterative solver was chosen to perform numerical simulations (Elman and Agron 1989). This solver was chosen because it provided similar performance as compared with the other solvers (within ANSYS, e.g. Frontal, Sparse, Jacobean conjugate gradient etc) at a relatively small computational time (Patil 2005). A grid of scatterers was defined over the 3D ROI of the simulated object (48 scatterers per resolution cell). The post-compression scatterer position was simulated by applying the 3D displacement field obtained from the FEA software to the scatterers.

It is worthwhile noting that the FEA simulations accounted not only for translational but also for rotational motion of an object due to any arbitrary boundary condition. Thus, realistic

---

[1] When the compressor plate is smaller in dimension than that of the compressed homogeneous object, the stress distribution in the object is non-uniform and is referred to as a non-uniform boundary condition at the object boundary (Sadda 1974).
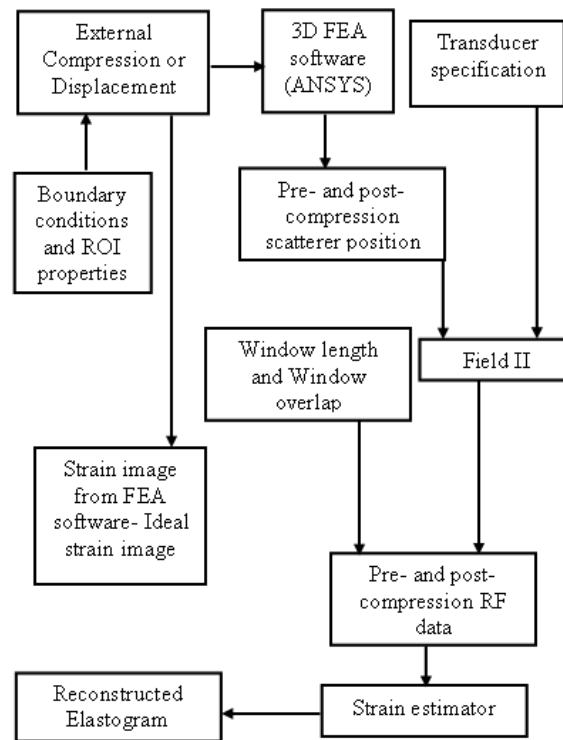
Figure 1. 3D elastographic simulation framework.

tissue motions can be simulated for arbitrary boundary conditions and arbitrary object shapes. Field II simulations were used to generate the pre- and post-compression echo RF data. The generated pre- and post-compression data can be tracked using different displacement (strain) estimation algorithms to generate a strain image. In this work, we used the strain estimation (signal processing) algorithm described in section 2.4.

2.2. Prostate phantom

All experiments were conducted on a purpose built prostate phantom. The acrylamide-based prostate phantom was fabricated using the protocol published by Negron *et al* (2002). The prostate phantom consisted of three compartments—the prostate tissue with embedded inclusion, the anal passage and the surrounding viscera. A schematic of the constructed phantom is illustrated in figure 2, whereas figure 3 illustrates a photographic view of the prostate phantom.

The prostate material and the surrounding gel (viscera) were composed of a 4% acrylamide solution, while inclusions in the prostates were composed of 8% acrylamide, which imparted different stiffness to the lesion and the surrounding prostate tissue. The Young's modulus for 4% gel is approximately 4 kPa, whereas it is 16 kPa in the 8% gel stiff inclusions (Konofagou *et al* 2003). Thus, the modulus ratio for all embedded lesions was approximately 4. Sephadex (GE-Amersham, Piscatway, NJ) was added to the prostates and inclusions to generate speckle; a higher concentration of sephadex was added to the inclusions than the surrounding prostates, thus yielding a different speckle pattern. Different speckle patterns were created to make
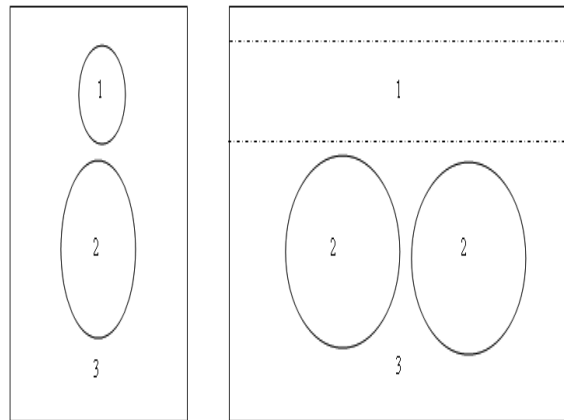
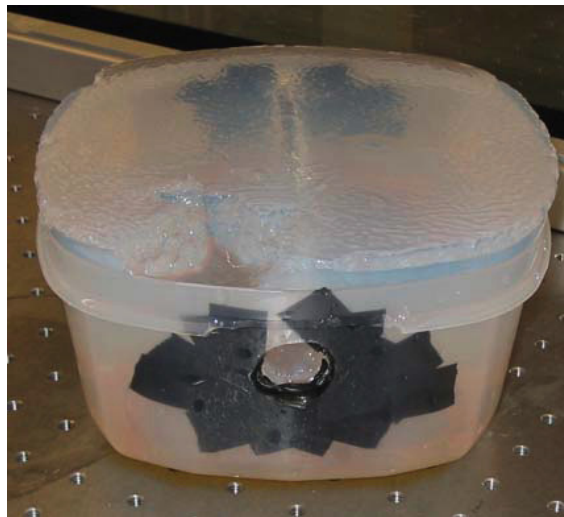**Figure 2.** Schematic of the prostate phantom. 1: anal passage, 2: prostate tissue, 3: viscera.

Figure 3. Prostate phantom—a photographic view.

inclusions visible on the sonogram, which enables comparison of 3D shape of inclusions reconstructed from elastograms and B-mode images. Two prostates of approximately 100 mL each were included in the phantom, one containing a spherical inclusion and the other containing an irregular inclusion. The smooth inclusion was approximately 8 mm in diameter whereas the irregular shaped inclusion had a mean diameter of 1 cm. To ensure uniform speckle pattern in inclusions and prostate, the mixture of different component solutions was enclosed in a latex balloon and was rolled gently for a setting period (approximately 20 min following the mixing of components) until the solution had solidified. The rolling protocol mitigates against the settling of the embedded inclusion and may sometimes lead to a situation where two inclusions are placed apposing each other, hence two different prostates were constructed, each embedding one inclusion.
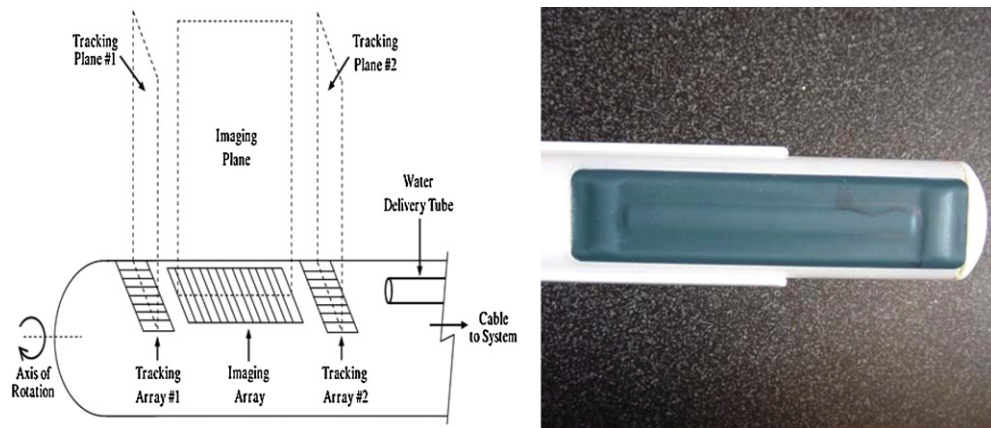
Figure 4. (a) Configuration of the 'I-Beam' transducer. (b) A photographic view of the prostate probe with tracking and imaging arrays.

2.3. I-Beam transducer

All experiments were conducted using a 512 Siemens Sequoia scanner and an 'I-Beam' array transducer. An 'I-Beam' (Hossack *et al* 2002) array transducer is a modified linear transducer array consisting of a central 'imaging' array bordered by two perpendicular 'tracking' arrays in a cylindrical housing, as illustrated in figures 4(a) and (b). The configuration allows for measuring the separation between two successive image slices by tracking the azimuthal motion in the tracking arrays while translating or rotating the 1D linear array. This simple modification in the 1D linear array enables 3D ultrasound imaging. A small tube for water delivery was attached to the transducer housing, and the assembly was surrounded with a water-tight latex transducer cover. This arrangement allowed for applying external compression by pumping the water in the latex transducer cover using a syringe.

2.4. Multi-resolution hybrid strain estimator

A complete flow chart of this strain estimation algorithm is illustrated in figure 5. In the first stage of our algorithm, we demodulate the RF data and track the envelope of the pre- and post-compression echo RF frames to yield average 'first-guess' strain estimates over the tracking window-W, where W is the length of the tracking window used for cross-correlation. The search range in this stage is one window length (on the either side along the axial direction) from the center of the tracking window. A fixed window overlap of 50% is used in this initialization stage. The tracking window in this stage is two times that in the subsequent RF tracking stages. The displacement obtained from this stage is referred to as the first stage axial displacement (^1D_a), where superscript '1' denotes the stage and subscript 'a' denotes the displacement type (here axial). Median filtering is used in all three stages to smooth the estimated displacements.

In the second stage, a fifth-order polynomial curve is fitted to the estimated local strain profile over each A-line, and the corresponding A-line is stretched by the curve-fitted first-stage strain.

Lateral displacement (^2D_l) is estimated by performing lateral tracking. When performing lateral tracking, the tracking window in the pre-compression data is searched for an optimum
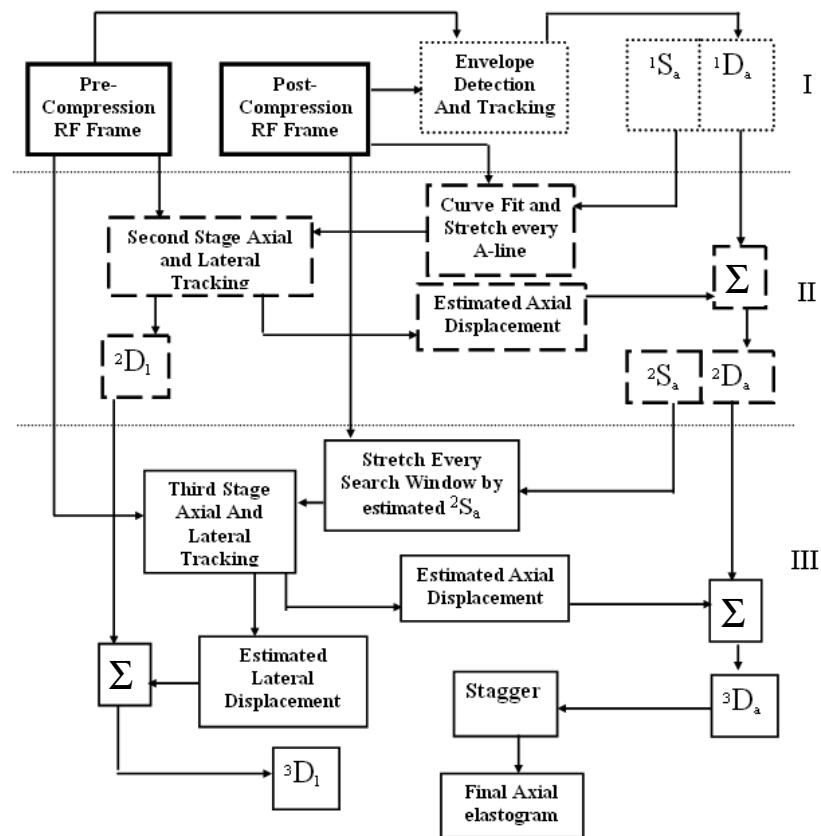
Figure 5. Flow chart of the new strain estimation algorithm. Note: dotted lined-rectangular boxes denote the first stage (I), whereas dashed lined-rectangular boxes signify the second stage (II), and solid lined-rectangular boxes represent the third stage (III).

match over the corresponding A-line and on three to five A-lines on the either side laterally. The maximum cross-correlation coefficients over these A-lines are estimated and a cosine curve (cosine interpolation) (Céspedes and Ophir 1993) is fitted to the data points. The shift in the peak of this curve in the transverse (lateral or azimuthal) direction yields the lateral displacement of the local pre-compression tracking window. Alternately, the A-lines can be interpolated or upsampled in the lateral direction before tracking (Konofagou *et al* 2000). The latter method provides finer lateral displacement estimates. The search ranges in the RF stages are obtained from the displacement estimates from previous stages. The axial displacement estimated in this stage is added to the first stage axial displacement and the resultant axial displacement is referred to as the second stage axial displacement (^2D_a).

The third stage is used to estimate residual strain. In the third stage, the original un-stretched post-compression RF data are stretched locally over a tracking window using the estimated second-stage strain. The stretched post-compression data are then tracked with the pre-compression data to yield residual axial displacements. The lateral displacements are obtained by tracking the A-lines laterally as detailed in the previous paragraph. The axial and lateral displacements estimated in this stage are added to the second stage axial and lateral displacement to yield the final axial (^3D_a), and lateral (^3D_l) displacements. In the last step of
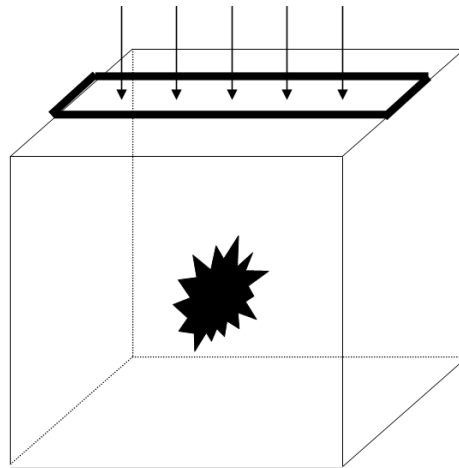
Figure 6. Schematic of the simulated phantom and imaging array used for CNR$_e$ study.

this algorithm, we apply the staggered strain estimation technique (Srinivasan *et al* 2002c) to the final stage axial displacement image to generate an elastogram. A staggered strain operator estimates strain over non-overlapping windows. For example, a window length of 2 mm and an overlap of 80% with an acquisition depth of 40 mm will yield approximately 100 pixels along the axial direction in a displacement image. A gradient operator will take a gradient [1 −1] over adjacent pixels and normalize it by the overlap and assign a strain value to the first pixel in a strain image. A staggered strain operator will take a gradient over the entire window, i.e. [1 0 0 0 0 −1] and normalize it by the window length assigning a strain value to the first pixel.

2.5. 3D elastographic simulations for performance evaluation and 3D rendering study

Elastographic simulations were performed using the framework described in section 2.1. Table 1 lists the simulation parameters used for performing various simulations described in this section. A cube ($40 \times 40 \times 40$ mm) enclosing a spiculated inclusion (10 mm diameter) was used as a mechanical model to simulate the background and the lesion was used for the CNR$_e$ (contrast-to-noise ratio) study (figure 6). The embedded inclusion (Young's modulus = 12 kPa) was simulated to be three times stiffer than the background (Young's modulus = 4 kPa).

A uniform cube-phantom was used for the SNR$_e$ (signal-to-noise ratio) study. The cubes were compressed axially from the top and assumed to be rested on a fixed surface such that their motions in the lateral and elevational directions were unconstrained (slip conditions). The cubes were compressed along the elevational axis of symmetry using a compressor plate (40×3 mm-lateral elevation plane) and the transducer array was placed over the compressor plate. The surface area of the compressor plate was smaller than the surface area of the top of the cube to simulate non-uniform boundary conditions at the top surface of the cube (figure 6). This results in non-uniform stress distribution through the depth of the tissue and consequently causes strain decay. The cube was subjected to a range of applied strain (0.5–10%). Pre- and post-compression RF data were generated using the 3D simulation framework detailed in subsection 2.1. The generated RF data were tracked using this proposed algorithm. Algorithms

Table 1. Simulation parameters.

Entity	Value
Dimensions of background	$40 \times 40 \times 40$ mm cube
Modulus ratio of inclusion and background	3 (12 and 4 kPa, respectively)
Approximate diameter of the inclusion	10 mm
Center frequency of scan	12 MHz
Sampling frequency	80 MHz
System SNR	30 dB
1D linear array	192 elements, 0.2 mm pitch
Focus	20 mm
Fractional bandwidth	40%
Window length (W)	2 mm
Overlap	90%

by Srinivasan *et al* (2002b) and by Céspedes and Ophir (1993) were also used to track the data for comparison with our algorithm. To be consistent, a stagger strain operator was used to generate elastograms from the displacement estimates obtained from all three methods. In Srinivasan *et al*'s (2002b) two-stage adaptive algorithm, the entire post-compression RF data are stretched by a single stretching coefficient (the underlying assumption here is that the stretching coefficient is known and the stress distribution is uniform) in the first stage.

The second stage is used for refining the displacements obtained from the first stage, lateral tracking is performed in both stages and lateral displacements are estimated. Céspedes and Ophir (1993) stretch the post-compression data by the applied global strain and track the pre- and post-compression data to create an elastogram. All three algorithms were compared based on SNR_e, CNR_e, correlation coefficient of the tracked pre- and post-compression signal, and variances in estimated strain values. Thirty independent realizations were used for each data point. Signal-to-noise ratio, variances and correlation coefficients were averaged over the entire image. Variances can be directly estimated from the correlation coefficient by using the expression in Walker and Trahey (1995) and are detailed in Srinivasan *et al* (2002a). CNR_e was calculated from the elastograms as follows,

$$CNR_e = \frac{\text{abs}(s_t - s_b)}{\sqrt{\frac{\sigma_t^2 + \sigma_b^2}{2}}} \tag{1}$$

where s_t is the average strain in the target and s_b is the average strain of the background. σ_t^2 is the variance of the strain estimates in the target, and σ_b^2 is the variance of the strain estimates in the background. A 5×5 pixel area was chosen within the inclusion, and a 5×5 area was chosen from the background diagonally two diameters away from the inclusion.

The 3D elastographic simulation framework described in section 2.1 was used to generate elastograms for 3D shape rendering and resolution study. The acoustic and signal processing parameters listed in table 1 were used in the rendering study. For the resolution study, the inclusions (one benign-spherical and one malignant-spiculated) were moved toward each other until they fused with each other. One malignant and one benign inclusion were considered to test the ability (best case) of the 3D elastographic technique to reconstruct different shapes. The spherical inclusion had a cross-sectional diameter of 5 mm, whereas the spiculated malignant inclusion had a mean cross-sectional diameter of approximately 6 mm. The inclusions were three times stiffer than the background. The rendering study was performed at an applied strain of 2%. The transducer array was swept along the elevational direction of the inclusions in steps of 1.2°, at each step a pre- and post-compression frame was acquired to generate

an elastogram. Twenty-three tomographic slices were generated in total to reconstruct the inclusions. Various elastograms obtained along the elevational direction were segmented using a 3D active surface constrained by gradient vector flow forces (GVFAS), as described in Xu and Prince (1998). The active contour model was initialized by manually selecting a series of circular 2D contours over the inclusions in various tomographic slices, which were interpolated to form a full 3D model. The model was deformed iteratively through space until convergence to a surface which satisfied the balance between internal active surface forces (tension and rigidity) and external forces imposed by a gradient vector flow field (computed from the 3D image data). The converged model was plotted in MATLAB using a 3D tessellation of the model vertices and rendered in 3D to reconstruct the 3D shapes of each inclusion. The strain images obtained directly from the FEA simulations were also segmented and rendered to produce ideal 3D shapes of the modeled inclusions. For the resolution study, the separation between the inclusions was reduced in steps of 0.1 mm. At every step the 3D shapes of the inclusions were reconstructed from the images. The process was repeated until the two inclusions were close enough to each other such that their reconstruction resulted in one fused entity instead of two distinct entities. The resolution was then defined as the absolute value of the difference between the sum of the average radii of the inclusions and the center-to-center distance between the two rendered inclusions.

2.6. 3D Elastographic experiments for performance evaluation and 3D rendering

Experimental evaluation of the tracking algorithm was performed on an acrylamide based prostate phantom previously fabricated by Li *et al* (2005). The mean cross-sectional diameter of the embedded oblong inclusion in the longitudinal (range) direction was approximately 7 mm. A Siemens Sequoia 512 scanner (Siemens Medical Solutions, Mountain View, CA) was used in this study. Multiple demodulated 'I/Q' (in-phase/quadrature) radio frequency beamformed lines of acoustic data were acquired from the ultrasound scanner using a research interface employing an I/Q data capture board. A 192 element, 12 MHz 40% fractional-bandwidth (-6 dB) trans-rectal 'I-Beam' ultrasound transducer was used for scanning the prostate phantom. The depth of acquisition was 24 mm and the width of acquisition was 40 mm. Fifty frames were acquired such that the total applied strain over 50 frames was approximately 2%. Every 25th frame (1 and 25-$E_{1,25}$, 2 and 26-$E_{2,26}$ and so on) was tracked. The final elastogram was generated by averaging over five independently obtained elastograms (($E_{1,25} + \cdots + E_{5,29}$)/5). The displacements were reconstructed using the proposed algorithm and algorithms by Srinivasan *et al* (2002b); a staggered strain operator was used to elastograms.

For 3D rendering, the prostate phantom described in section 2.2 was scanned using an 'I-Beam' type transducer. Using this configuration, the angular separation between two successive image slices could be tracked by measuring the azimuthal motion in the tracking arrays. This assembly was mounted so that during the angular rotation, translational motion was restricted, facilitating pure rotational motion of the transducer. The mounted transducer was inserted into the prostate phantom and rotated to perform a series of two-dimensional elastographic scans. At every angular position, the phantom was compressed by injecting water in the transducer sheath via the connected tube using a syringe pump while simultaneously collecting fifty I/Q data frames. For each lesion, gain, field of view and focal depth were optimized for maximum visibility of that particular lesion. Sixteen tomographic slices were collected across each inclusion ($\sim 1.5°$ elevational separation). The data were processed offline as detailed in section 2.5 to generate elastographic image slices. Various elastograms obtained along the elevational direction were segmented using the 3D gradient vector flow active surface (GVF-AS) algorithm and rendered in 3D to reconstruct the 3D shapes of the inclusions.
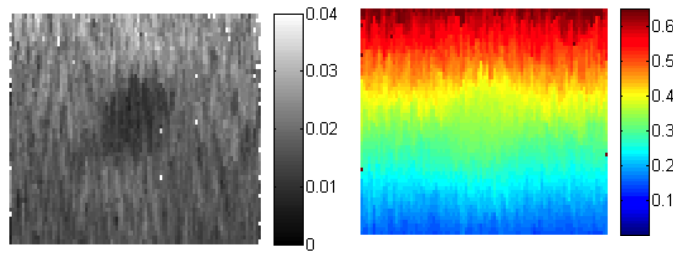
Figure 7. First stage elastogram (left) and axial displacement image (right). The field of view is 40 × 40 mm.
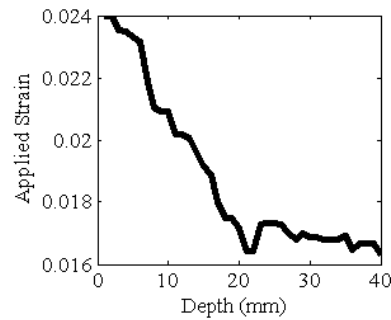

Figure 8. Strain profile over an A-line in the elastogram (figure 7, left) obtained by the B-mode tracking.
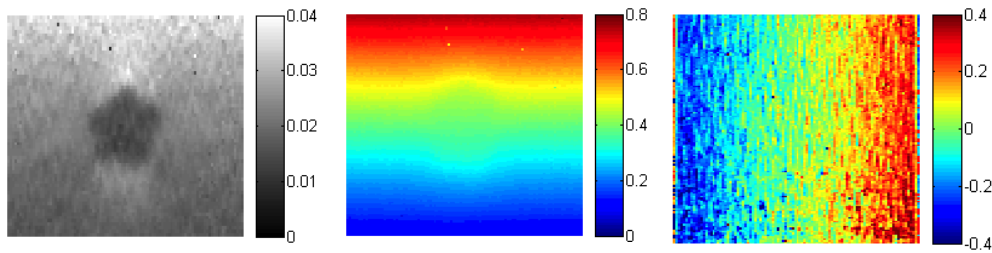

Figure 9. Second stage elastogram (left), axial displacement image (center), lateral displacement image (right). The field of view is 40 × 40 mm.

3. Results

Figures 7–10 illustrate the elastograms generated at various stages using the proposed algorithm. Figure 11 represents the numerical strain image or ideal elastogram from the FEA software.

Figures 7–11 were obtained using parameters in table 1. Figure 12 illustrates the signal-to-noise ratio (SNR_e) plots obtained using different tracking approaches. Thirty independent realizations were used to generate the error bars in the plot. The SNR_e plot obtained using the proposed algorithm envelopes the SNR_e plots obtained using other algorithms. For all values of applied strain, the SNR_e plot obtained using the proposed algorithm was statistically
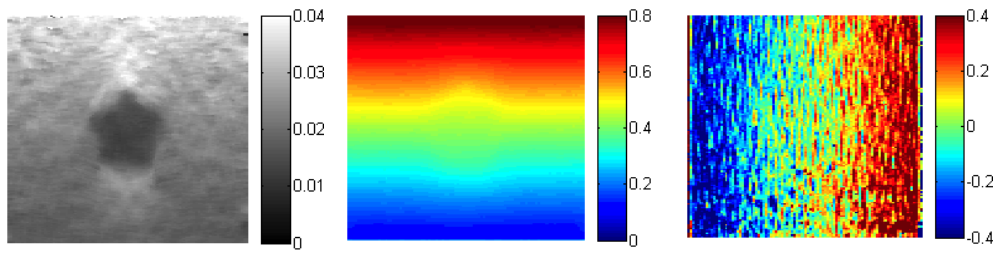
Figure 10. Final stage elastogram (left), axial displacement image (center), lateral displacement image (right). The field of view is 40×40 mm.
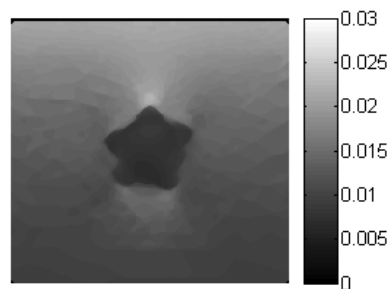

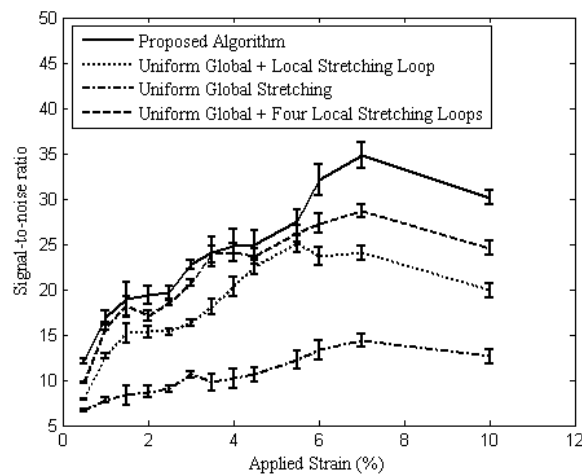**Figure 11.** Ideal strain image obtained from the FEA simulations.

Figure 12. SNR$_e$ plot for different tracking approaches. Error bars represent one standard deviation.

different ($p < 0.05$) from those obtained using Srinivasan *et al*'s (2002b) algorithm. Analysis of variance was used as a statistical measure to quantify the difference between two curves. Variances in the SNR$_e$ calculation were generated directly from the correlation coefficients as detailed in Srinivasan *et al* (2002a). Figure 13 illustrates the average image variance calculated over the entire image at different values of applied strain. As predicted by the strain filter
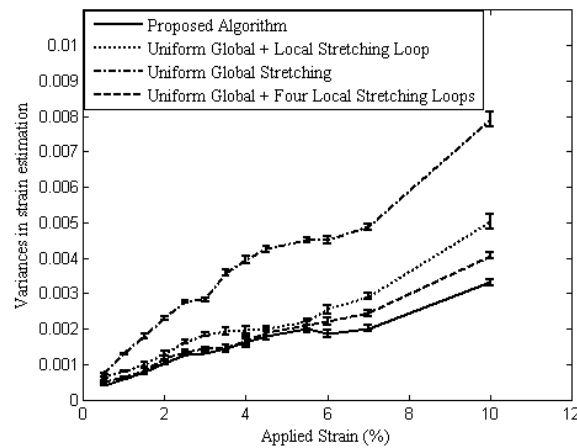
Figure 13. Estimated image variance comparing different tracking approaches. Error bars represent one standard deviation.
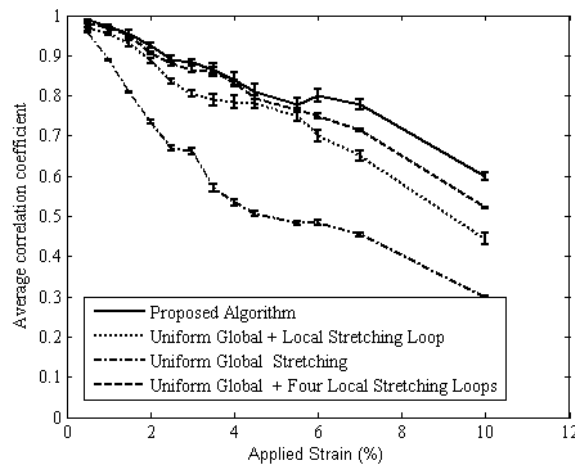

Figure 14. Average cross-correlation coefficient over the reconstructed image obtained using different tracking approaches. Error bars represent one standard deviation.

theory (Varghese and Ophir 1997), variances in strain estimation increase nonlinearly with applied strain. The rate of increase in variance is lowest when using the proposed algorithm. Figure 14 illustrates the average cross-correlation coefficient (ρ) over the image obtained using different tracking algorithms. The error bars in figure 14 illustrate the variance in the average image cross-correlation coefficient obtained from 30 independent realizations. The rate of decrease in the correlation coefficient as a function of applied strain is smallest for the proposed algorithm. Figure 15 illustrates different contrast-to-noise ratio curves (CNR_e) obtained from the elastograms simulated using different strain estimation algorithms. CNR_e values for a range of applied strains (0.5–10%) obtained using the proposed algorithm are 3 dB above the CNR_e curve obtained using the algorithm proposed by Srinivasan *et al* (2002b) and are 6 dB higher than the RF data tracking algorithm with uniform global stretching (Céspedes
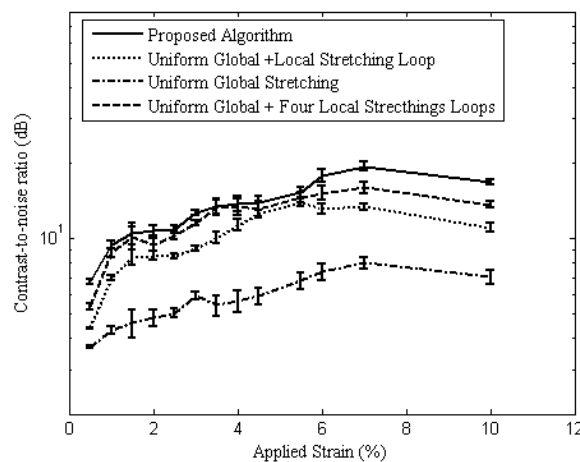
Figure 15. CNR$_e$ plots obtained using different tracking approaches. Error bars represent one standard deviation.
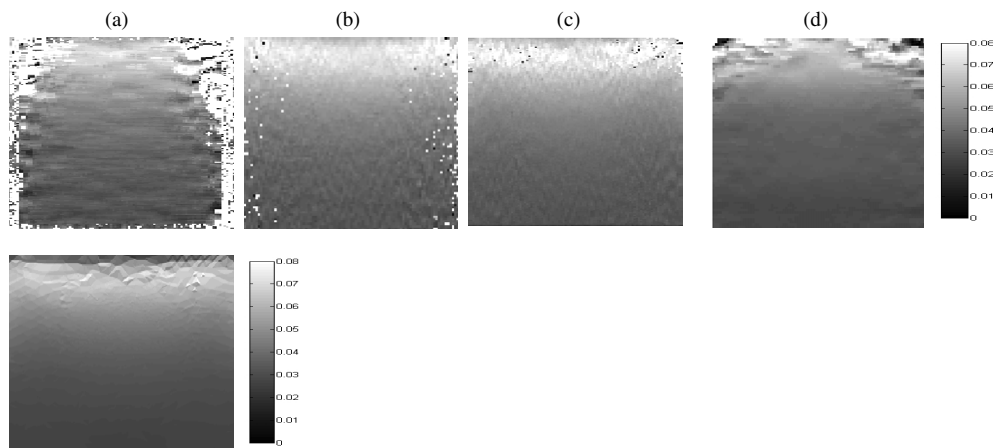

Figure 16. Top row—elastograms. (a) Uniform global stretching, (b) global + local stretching, (c) global + four local stretching iterations, (d) proposed method. Bottom row—ideal strain image. Note: all elastograms were generated using a stagger operator.

and Ophir 1993). However, it is worthwhile noting that similar elastographic image quality can be obtained by modifying Srinivasan *et al*'s (2002b) algorithm by iterating the local loop multiple times. As illustrated in figures 12–15, no statistical difference was observed between the images generated using the proposed algorithm and modified Srinivasan *et al*'s (2002b) algorithm (four local iterations) for an applied strain of <5%. Figures 16 and 17 illustrate elastograms generated using (a) global stretching approach, (b) Srinivasan *et al*'s (2002b) approach, (c) Srinivasan *et al*'s (2002b) approach with local stretching loop iterated four times and (d) with the proposed algorithm. All images were generated at an applied strain of 4%. To be consistent all strain images were generated using a stagger operator (Srinivasan *et al* 2002c) rather than a gradient operator. Comparable image quality can be obtained using the modified
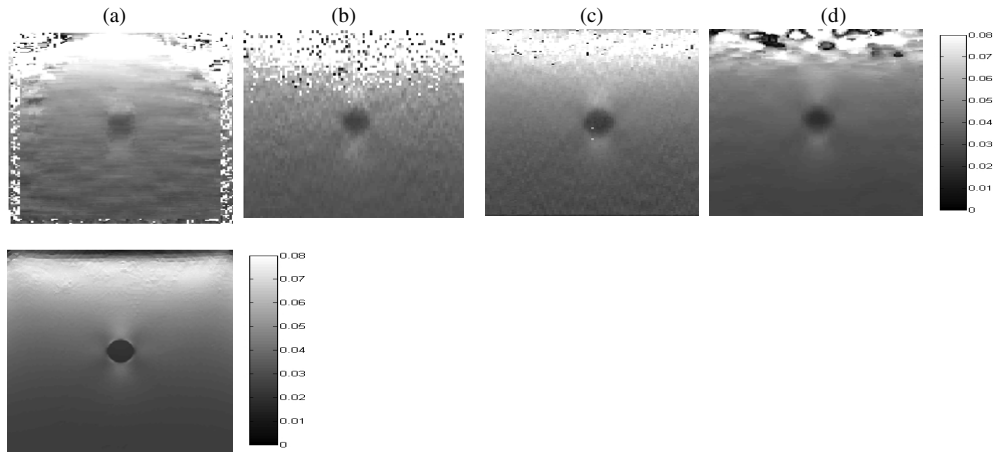
Figure 17. Top row—elastograms. (a) Uniform global stretching, (b) global + local stretching, (c) global + four local stretching iterations, (d) proposed method. Bottom row—ideal strain image. Note: all elastograms were generated using a stagger operator.
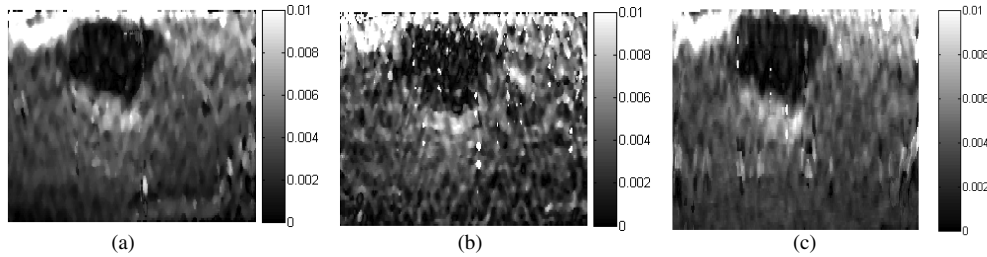

Figure 18. Elastogram generated using (a) proposed method, (b) the algorithm by Srinivasan *et al* (2002b), (c) the algorithm by Srinivasan *et al* (2002b) with the local loop iterated three times. All elastograms were generated using a stagger strain operator (Srinivasan *et al* 2002c).

Srinivasan *et al*'s (2002b) algorithm by iterating the local loop four times. The demand for local iterations, however, increases with increasing strains.

Figure 18(a) illustrates an elastogram obtained using the method proposed in this paper. Figure 18(b) illustrates an elastogram reconstructed by using the algorithm proposed by Srinivasan *et al* in (2002b). Figure 18(c) illustrates an elastogram generated by modifying Srinivasan *et al*'s (2002b) algorithm by iterating the local loop three times. All three elastograms were generated using a stagger operator. As illustrated in figures 18(a) and (b), elastograms generated by the algorithm proposed in this paper provide higher CNR_e and retain the shape of the enclosed inclusion.

Similar results are obtained by modifying Srinivasan *et al*'s (2002b) algorithm by increasing the number of local iterations. One likely cause of a reduced CNR_e in figure 18(b) is the uniform stress distribution assumption, and the lack of the knowledge of an exact stretching coefficient in the hand-held elastographic experiments thus resulting in a non-optimal initialization of Srinivasan *et al*'s (2002b) algorithm. The algorithm proposed in this paper stretches every A-line by the local strain profile over that A-line as predicted by the B-mode tracking stage thus accounting for the strain decay with depth and hence minimizes
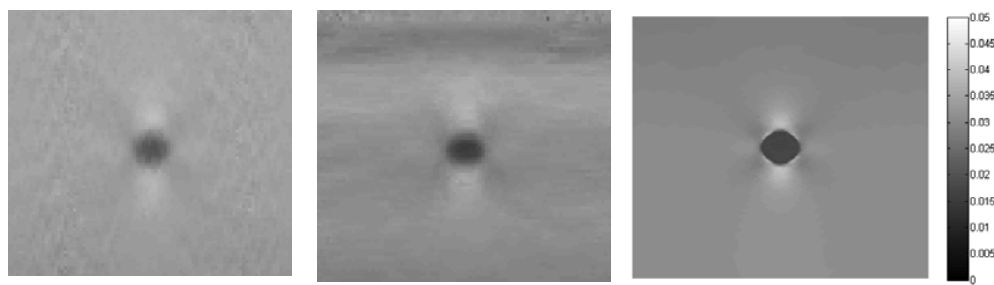
Figure 19. Left: elastogram using Srinivasan *et al* (2002b, 2002c), center: elastogram using the proposed method, right: analytical strain image. Elastograms were generated using parameters mentioned in table 1, at 3% applied compression using uniform boundary conditions.

the increased number of iterations required in Srinivasan *et al*'s (2002b) algorithm for producing equivalent results. Thus, for trans-rectal and hand-held elastography, the proposed algorithm is expected to exhibit superior performance to Srinivasan *et al*'s (2002b) algorithm and similar performance to the modified (multiple local loop iterations) Srinivasan *et al*'s (2002b) algorithm but at a reduced computational cost. For the case with uniform boundary condition and where the applied strain is known *a priori*, we expect that both algorithms should demonstrate similar performance (figure 19). Figure 20 illustrates the 3D reconstruction from the axial resolution study. The axial resolution of the 3D reconstruction was approximately 0.8 mm (five wavelengths). Figures 20(a) and (d) illustrate a 3D reconstruction from the generated elastograms, whereas figures 20(b) and (c) illustrate a 3D reconstruction from the ideal numerical strain images obtained from the FEA simulations. As expected, the 3D reconstruction from ideal images is sharper than that from the elastogram. Also, the lesions reconstructed from the elastogram exhibit shape warping that can be attributed to limitations arising from the signal processing parameters (window length and window overlap, etc), and non-uniformity of sampling of the ultrasound data in the three dimensions (Patil *et al* 2007). The lateral resolution of the 3D reconstruction was approximately 1.5 mm (ten wavelengths). Figure 21 illustrates elastograms and corresponding sonograms for a few angular positions of the trans-rectal prostate transducer while sweeping across the irregular shaped inclusion. Figure 22 illustrates similar images for the smooth shaped inclusion. Figure 23 illustrates images of the smooth and irregular shaped inclusions reconstructed from sonograms and elastograms, respectively. The shape and the size of the smooth inclusion reconstructed from the sonograms and elastograms are approximately similar. The smooth inclusion reconstructed from elastograms tapers at the longitudinal edges, probably due to the low pass filtering or smoothing effect of the processing windows used for generating elastograms. The irregular shaped inclusion reconstructed from the elastograms has blunt edges and appears larger in size than that reconstructed from the sonogram or B-mode image and may be attributed to the processing window used in tracking the signals. Thus, we contend that the 3D elastography has the potential to assist in discriminating benign lesions from malignant cancers.

4. Discussion

In elastography, the image quality is contingent upon an accurate estimation of internal tissue displacements. In displacement estimation, cross-correlation between pre- and post-compression signals is maximized when two signals are jointly stationary. In addition, if the time–bandwidth product is large and the shifts in the signal are small, cross-correlation is
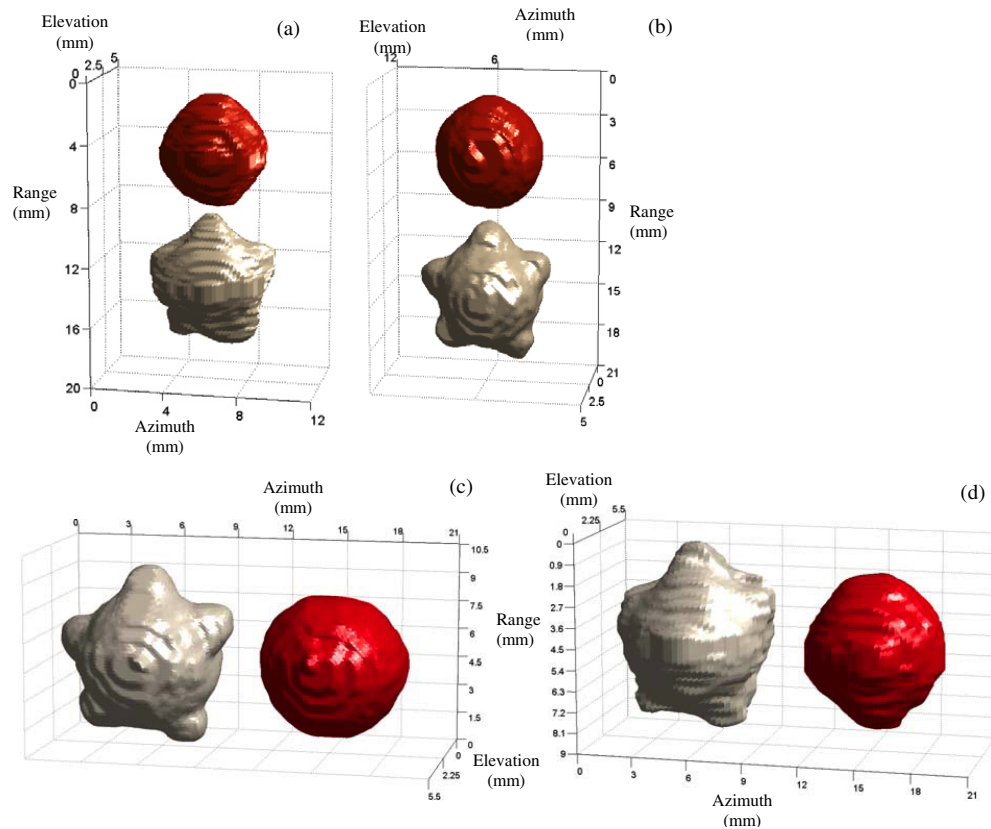
Figure 20. 3D reconstruction from FEA ((b), (c)) models and reconstructed elastograms ((a), d)) where (a) and (b) are from axial resolution and (c) and (d) are from lateral resolution study.
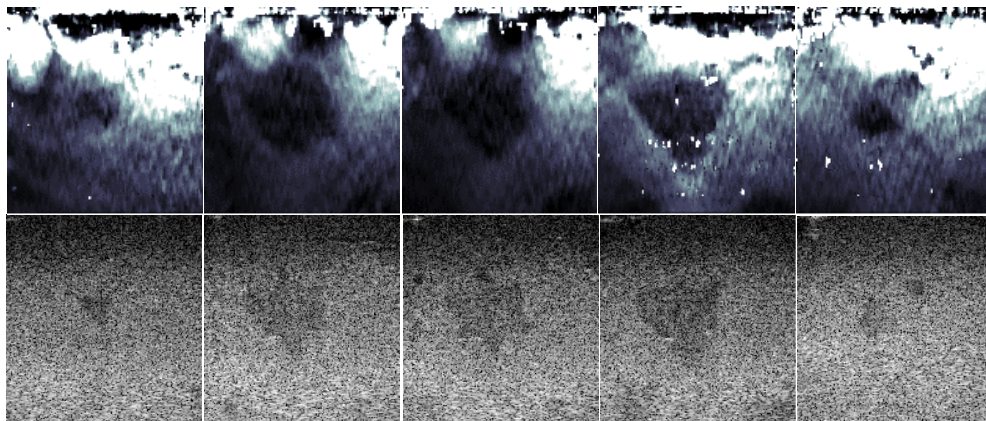

Figure 21. A few slices across the embedded inclusion mimicking a malignant lesion. The top row illustrates elastograms, the bottom row illustrates sonograms. The field of view is 30 × 30 mm.

an efficient estimator of displacement (hence strain) and in the limit achieves the Cramer–Rao lower bound on variance. However in practice, the pre- and post-compression signals
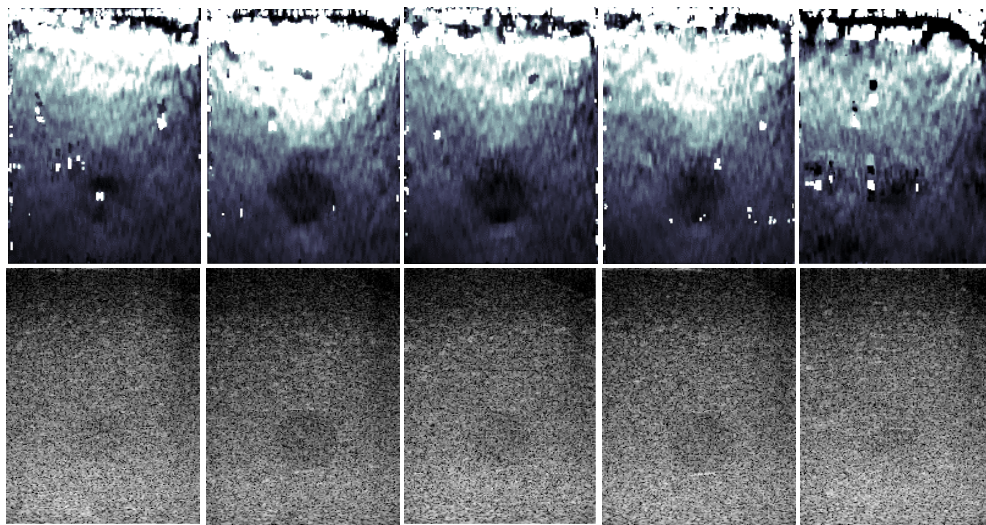
Figure 22. A few slices across the embedded inclusion mimicking a benign lesion. The top row illustrates sonograms, the bottom row illustrates elastograms. The field of view is 40×30 mm.

are jointly non-stationary. Hence, signal companding (Chaturvedi *et al* 1999) or stretching (Céspedes and Ophir 1993) is frequently used to improve image quality. Signal companding is a simple yet an elegant approach of improving elastographic image quality. In this paper, we proposed an adaptive stretching based tracking algorithm. In the first stage of this strain estimation algorithm we use a B-mode tracking stage, which automatically and locally initializes the algorithm. If the applied strain is large (>2%, for a ∼4 cm deep prostate tissue imaged at 12 MHz), the induced displacement is sufficiently larger than the wavelength corresponding to center frequency and may introduce ambiguity in peak detection of the cross-correlation function obtained by tracking the pre- and post-compression RF data. Thus, an induction of a B-mode tracking stage not only enables local initialization, but also helps in increasing the dynamic range of the elastograms. The subsequent nonlinear and linear tracking stages enable faster convergence of the algorithm, thus reducing the total computation time. Typical advantages of this algorithm over Srinivasan *et al*'s (2002b) approach are: (a) the algorithm is independent of manual initialization (*a priori* knowledge of applied strain) and (b) it produces equivalent or better results in fewer numbers of iterations. This difference is clearly evident especially at higher strains. In the final stage of this algorithm, we use a stagger strain operator against a gradient or a least-squares operator (Kallel and Ophir 1997). A gradient operator is a high pass operator and amplifies noise. A least-squares filter typically performs low pass filtering thus mitigating the image contrast. A stagger operator plays an intermediate role of being a band pass filter limiting the noise amplification while providing smooth elastograms and minimizing the loss in contrast and resolution. One disadvantage of correlation based multi-stage adaptive algorithms is enormous computation time. For high frame rate real-time hand-held elastography, the proposed algorithm may be modified to reduce the computation time. For example, the correlation based tracking in the first two stages of this algorithm may be replaced by a sum-of-absolute-difference approach (Chaturvedi *et al* 1999), whereas the third stage may be replaced by temporal tracking of zero crossings of the pre- and post-compression echo RF signals. Thus, a reduction in computation time may be achieved by an order of magnitude without any substantial degradation in image quality.
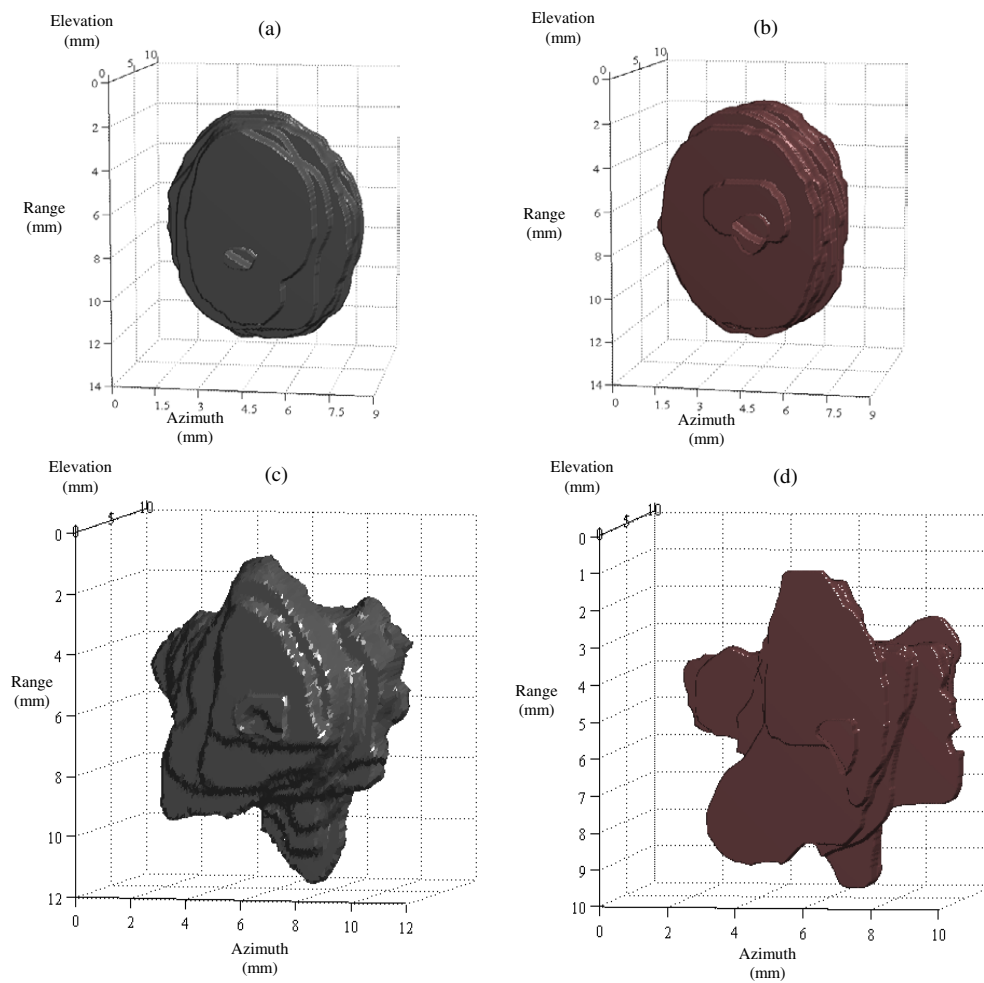
Figure 23. (a) Smooth inclusion mimicking a benign lesion reconstructed from elastograms. (b) Smooth inclusion reconstructed from sonograms. (c) Irregular shaped inclusion mimicking a malignant lesion reconstructed from elastograms. (d) Irregular shaped lesion inclusion reconstructed from sonograms.

The modified 3D elastographic simulation framework proposed in this work may prove useful in performing realistic 3D simulations for techniques such as shear strain elastography and poroelastography, where designing multi-parametric experiments may be complicated. This simulation framework uses a FIELD II model for generating the RF data; FIELD II is computationally expensive, and hence may be replaced by a recently proposed Field II variant called DELFI (Ranganathan and Walker *et al* 2007) to obtain similar results at a fraction of the computation time. Recent induction of 2D array transducers in diagnostic ultrasound has enabled fast and real-time 3D ultrasound imaging. 2D array transducers have been demonstrated to perform 3D IVUS imaging (Light and Smith 2003). This technology can be easily incorporated into a trans-rectal transducer and may provide advantages such as dynamic transmit and receive focusing of the ultrasound beam in the elevation and uniform sampling of RF data in azimuth and elevation, enabling substantial improvement in the image quality by precisely estimating non-axial components of the strain tensor. Such 3D elastography imaging

systems may be used for a variety of applications such as real-time volumetric monitoring of HIFU lesions (Souchon *et al* 2005) and real-time volumetric estimation of viscous properties of tissue (Erpelding *et al* 2005). A very high frequency modified version of this 3D elastography system may prove useful in oncology studies using small animal human disease models (e.g. mice), typically for monitoring growth and proliferation of cancers.

References

American Cancer Society 2006 Statistics from www.cancer.org
Bilgen M and Insana M F 1997 Predicting target detectability in acoustic elastography *Proc. IEEE Ultrason. Symp.* **2** 1427–30
Bilgen M, Srinivasan S, Lachman L B and Ophir J 2003 Elastography imaging of small animal oncology models: a feasibility study *Ultrasound Med. Biol.* **29** 1291–6
Céspedes I and Ophir J 1993 Reduction of image noise in elastography *Ultrason. Imaging* **15** 89–102
Chaturvedi P, Insana M F and Hall T J 1999 2-D companding for noise reduction in strain imaging *IEEE Trans. Ultrason. Ferroelectr. Freq. Control* **45** 179–91
Elkis M J and Brawer M K 1994 The significance of iso-echoic prostate carcinomas *Urology* **152** 2304–7
Elman H C and Agron E 1989 Ordering techniques for pre-conditioned conjugate gradient method on parallel computers *Comput. Phys. Commun.* **53** 253–69
Erpelding T N, Hollman K W and O'Donnell M 2005 Bubble-based acoustic radiation force elasticity imaging *IEEE Trans. Ultrason. Ferroelectr. Freq. Control* **52** 971–9
Fellepa E J *et al* 2001 Spectrum-analysis and neural networks for imaging to detect and treat prostate cancer *Ultrason. Imaging* **23** 135–3146
Garra B S, Céspedes I, Ophir J, Spratt S, Zuurbier R A, Magnant C M and Pennanen M F 1997 Elastography of breast lesions: initial clinical results *Radiology* **202** 79–86
Halpern E J, MCcue P A, Aksnes A K, Hagen E K, Frauscher F and Gomella L G 2002 Contrast-enhanced US of prostate with Sonazoid: comparison with whole-mount prostatectomy specimens in 12 patients *Radiology* **222** 362–6
Hossack J A, Sumanaweera T S, Napel S and Ha J S 2002 Quantitative 3D diagnostic ultrasound imaging using a modified transducer array and an automated image tracking technique *IEEE Trans. Ultrason. Ferroelectr. Freq. Control* **49** 1029–38
Jensen J A and Nikolov I 2000 Fast simulations of ultrasound images *Proc. IEEE Ultrason. Symp.* **2** 1721–4
Kallel F and Ophir J 1997 A least squares estimator for elastography *Ultrason. Imaging* **19** 195–208
Konofagou E E, Ottensmeyer M, Dawson S L and Hynynen K 2003 Harmonic motion imaging—applications in detection of stiffer masses *Proc. IEEE Ultrason. Symp.* pp 558–61
Konofagou E E, Varghese T and Ophir J 2000 Theoretical bounds on the estimation of transverse displacement, transverse strain and Poisson's ratio in elastography *Ultrason. Imaging* **22** 153–77
Krouskop T A, Wheeler T M, Kallel F, Garra B S and Hall T 1998 Elastic moduli of breast and prostate tissues under compression *Ultrason. Imaging* **20** 260–74
Li Y, Patil A V and Hossack J A 2005 Combined elasticity and 3D imaging of the prostate *Proc. IEEE Ultrason. Symp.* **3** 1435–8

Light E D and Smith S W 2003 Two dimensional array for real-time 3D intravascular ultrasound *Proc. IEEE Ultrason. Symp.* **3** 877–80

Negron L A, Viola F, Black E P, Toth C A and Walker W F 2002 Development and characterization of a vitreous mimicking material for radiation force imaging *IEEE Trans. Ultrason. Ferroelectr. Freq. Control* **49** 1543–51

Nightingale K R, Nightingale R W, Palmeri M L and Trahey G E 2000 A finite element model of remote palpation of breast lesions using ultrasonic radiation force: factors affecting tissue displacement *Ultrason. Imaging* **22** 35–54

O'Donnell M, Skovoroda A R, Shapo B M and Emelianov S Y 1994 Internal displacement and strain imaging using ultrasonic speckle tracking *IEEE Trans. Ultrason. Ferroelectr. Freq. Control* **41** 314–25

Ophir J, Céspedes I, Ponnekanti H, Yazdi Y and Li X 1991 Elastography: a method for imaging the elasticity of biological tissue *Ultrason. Imaging* **13** 111–34

Patil A V 2005 Quantitative comparison of 2D and 3D elastograms: a simulation study *Masters' Thesis* University of Houston

Patil A V, Krouskop T A, Ophir J and Srinivasan S 2007 On the effect of 3D tissue motion on ultrasound elastography: a simulation study *Ultrasound Med. Biol.* in preparation

Pesavento A and Lorenz A 2001 Real time strain imaging and in-vivo application in prostate cancer *Proc. IEEE Ultrason. Symp.* **2** 1647–52

Potdevin T, Moskalik A, Rubin M, Bree R and Carson P 2000 Zonal analysis of 3D ultrasound Doppler quantitative measure for the discrimination of prostate cancer *Proc. IEEE Ultrason. Symp.* **2** 1321–4

Ranganathan K and Walker W F 2007 Cystic resolution: a performance metric for ultrasound imaging systems *IEEE Trans. Ultrason. Ferroelectr. Freq. Control* **54** 782–92

Righetti R, Ophir J and Ktonas P 2002 Axial resolution in elastography *Ultrasound Med. Biol.* **28** 101–13

Sadda A S 1974 *Elasticity Theory and Application* (New York: Pergamon) pp 395–428

Sheppard M A and Shih L 2005 Efficient image texture analysis and classification for prostate cancer diagnosis *Proc. IEEE Computational Systems Workshop*

Souchon R, Bouchoux G, Maciejko E, Lafon C, Bertrand M and Chapelon J Y 2005 Monitoring the formation of thermal lesions with heat-induced echo-strain imaging: a feasibility study *Ultrasound Med. Biol.* **31** 251–9

Srinivasan S, Kallel F and Ophir J 2002a Estimating the elastographic signal-to-noise ratio using correlation coefficients *Ultrasound Med. Biol.* **28** 359–68

Srinivasan S, Kallel F, Souchon R and Ophir J 2002b Analysis of an adaptive strain estimation technique in elastography *Ultrason. Imaging* **24** 109–18

Srinivasan S, Ophir J and Alam S K 2002c Elastographic imaging using staggered strain estimates *Ultrason. Imaging* **25** 229–45

Techavipoo U, Chen Q, Varghese T and Zagzebski J A 2004 Estimation of displacement vectors and strain tensors in elastography using angular insonifications *IEEE Trans. Med. Imaging* **23** 1479–84

ThitaiKumar A, Ophir J and Krouskop T A 2005 Noise performance and signal-to-noise ratio of shear strain elastograms *Ultrason. Imaging* **27** 145–65

Ueno E 1986 Classification and diagnostic criteria in breast echography *Japan. J. Med. Ultrason.* **13** 19–31

Varghese T and Ophir J 1997 A theoretical framework for performance characterization of elastography: the strain filter *IEEE Trans. Ultrason. Ferroelectr. Freq. Control* **44** 164–72

Walker F W and Trahey G E 1995 A fundamental limit on delay estimation using partially correlated speckle signals *IEEE Trans. Ultrason. Ferroelectr. Freq. Control* **42** 301–8

Waterhouse R L and Resnick M I 1989 The use of trans-rectal prostatic ultrasonography in the evaluation of patients with prostatic carcinoma *Urology* **141** 233–9

Xu C and Prince J L 1998 Snakes, shape and gradient vector flow *IEEE Trans. Image Proc.* **7** 359–69